Liu, W.-J., Wang, H., Lee, J., Kwon, E., Xuan Thanh, B., You, S. , Park, Y.-K., Tong, S. and Andrew Lin, K.-Y. (2021) Investigating crystal plane effect of Co3O4 with various morphologies on catalytic activation of monopersulfate for degradation of phenol in water. *Separation and Purification Technology*, 276, 119368. (doi: 10.1016/j.seppur.2021.119368)

There may be differences between this version and the published version. You are advised to consult the published version if you wish to cite from it.

http://eprints.gla.ac.uk/248789/

Deposited on 3 August 2021

Investigating crystal plane effect of Co_3O_4 with various morphologies on catalytic activation of Monopersulfate for degradation of Phenol in Water

Wei-Jie Liu[a], Haitao Wang[b], Jechan Lee[c], Eilhann Kwon[d] Bui Xuan Thanh[e], Siming You[f], Young-Kwon Park, Shaoping Tong[g,*]and Kun-Yi Andrew Lin[a,*]

[a]Department of Environmental Engineering & Innovation and Development Center of Sustainable Agriculture, National Chung Hsing University, 250 Kuo-Kuang Road, Taichung, Taiwan

[b]Key Laboratory of Pollution Processes and Environmental Criteria, College of Environmental Science and Engineering, Nankai University, Tianjin 300071, P. R. China

[c] Department of Environmental and Safety Engineering, Ajou University, Suwon 16499, Republic of Korea

[d]Department of Environment and Energy, Sejong University, 209 Neungdong-ro, Gunja-dong, Gwangjin-gu, Seoul, Republic of Korea

[e]Faculty of Environment and Natural Resources, Ho Chi Minh City University of Technology, VNU-HCM, 268 Ly Thuong Kiet, District 10, Ho Chi Minh City, 700000, Viet Nam

[f]James Watt School of Engineering, University of Glasgow, Glasgow G12 8QQ, UK

[g]College of Chemical Engineering, State Key Laboratory Breeding of Green Chemistry-Synthesis Technology, Zhejiang University of Technology, Hangzhou 310032, China

*Corresponding Authors. E-mail address:linky@nchu.edu.tw; sptong@zjut.edu.cn

1

Abstract

As phenol represents as the most typical persistent organic pollutants in wastewater, $SO_4^{\bullet-}$-involved chemical oxidation techniques using monopersulfate (MPS) have been regarded as a promising method to eliminate phenol. Since Co_3O_4 is the benchmark heterogeneous catalyst for activating MPS, it is highly critical to investigate shape-varied Co_3O_4 catalysts with well-defined crystal planes for activating MPS to degrade phenol. Thus, the aim of this study is to elucidate how different Co_3O_4 catalysts with various well-defined planes would influence catalytic activities for MPS activation. Specifically, three Co_3O_4 nanocrystals are fabricated: nanoplate (NP), nanobundle (NB), and nanocube (NC) with different dominant exposed facets of {112}, {110}, and {100}, respectively. As the facets of {112} and {110} consist of more abundant Co^{2+}/Co^{3+}, Co_3O_4-NP and Co_3O_4-NB exhibit noticeably higher catalytic activities then Co_3O_4-NC for activating MPS to degrade phenol. Nevertheless, since Co_3O_4-NP shows a much higher surface area than Co_3O_4-NB, Co_3O_4-NP could exhibit a relatively high catalytic activity in comparison to Co_3O_4-NB. In addition, Co_3O_4-NP also exhibits much faster degradation kinetics with a rate constant of 0.061 min^{-1} at 30°C, and more resistance towards pH variation, with much stable reaction stoichiometric efficiencies (RSE) ranging from 0.034 to 0.039 at pH = 3~9, than the other two Co_3O_4 nanocrystals, making Co_3O_4-NP with the {112} facet a more outstanding Co_3O_4 for activating MPS to degrade phenol.

1. Introduction

Among organic pollutants in wastewater discharged from industrial processes [1], phenol is one of the most typical pollutants. As phenol is a persistent organic pollutant, it has been classified as a class II water hazard, and thus its concentrations in effluents and even drinking water are strictly regulated [2]. However, due to its low biodegradability and toxicity [3], elimination of phenol would usually necessitate more intensive physico-chemical processes to avoid adverse effects of phenol on the environment and ecology. Therefore, several techniques have been proposed to eliminate phenol from polluted water, including membrane filtration [2], adsorption [4], photo-degradation [5], and chemical oxidation [6-10]. Among these techniques, chemical oxidation appears as the most useful one because chemical oxidation can rapidly oxidize organic pollutants, leading to decomposition of phenol, and thus chemical oxidation receives growing interests for phenol degradation.

In general, most of conventional chemical oxidation techniques are hydroxyl radical ($^\bullet$OH)-involved techniques, such as Fenton's reaction. However, sulfate radical ($SO_4^{\bullet-}$)-involved chemical oxidation techniques also attract increasingly attention recently because $SO_4^{\bullet-}$ possesses several advantages over $^\bullet$OH [11-14], namely, higher oxidation potentials, longer half-lives and higher selectivities [15-17]. Therefore, it would be more promising to develop useful $SO_4^{\bullet-}$-based processes to degrade phenol. To this end, monopersulfate (MPS) is frequently adopted as a source agent of $SO_4^{\bullet-}$ because MPS is environmentally benign, inexpensive and easily-accessible [18]. Nonetheless, auto-generation of $SO_4^{\bullet-}$ from MPS is very slow and thus catalysts are usually required to activate MPS for quickly generation of $SO_4^{\bullet-}$ speedily [15-17, 19].

Recently, several metals have been proposed for activating MPS to degrade phenol in water, such Ce [20], Mn [21], Co [8, 22-24], Fe [25], Cu [26], etc. For instance,

Othman et al. have attempted to CeVO$_4$ for activating PMS to degrade phenol with relatively high concentrations of PMS and CeVO$_4$ [2]. Besides, manganese-based catalysts, such as LaMnO$_3$ [3], MnO$_2$ molecular sieve [4], and MnO$_2$ nanoparticles [5], are also extensively employed for activating PMS to degrade phenols. On the other hand, N-doped carbon, without any metal content, is also developed for activating PMS to degrade phenol [6].

Nevertheless, among these catalysts, Co has been proven as the most effective metal for activating MPS to degrade organic pollutants. Thus various types of Co-containing heterogeneous catalysts have been proposed to activate MPS to degrade phenol, such as coal ash/Co$_3$O$_4$ [8], Co/SBA-15 [23], Co/Fe bimetallic oxides [25], CuO-Co$_3$O$_4$@MnO$_2$ [26], Co$_3$O$_4$/MnO$_2$ [22], Co/CeO$_2$ [24], etc. Most of these catalysts are fabricated by combining Co$_3$O$_4$ with other constituents as Co$_3$O$_4$ is validated as the benchmark heterogeneous catalyst for MPS activation [27, 28]. Nevertheless, there are various types of Co$_3$O$_4$ in terms of sizes, shapes, morphologies, and structures. Moreover, crystal planes of metal oxides are also strongly associated with their catalytic activities [29-31]. Thus, it would be highly crucial to investigate shape-varied Co$_3$O$_4$ catalysts with well-resolved crystal planes for activating MPS to degrade phenol to provide deeper understanding and insights for designing optimal Co$_3$O$_4$ catalysts. However, very few studies exist in literature for examining the relationship between morphology, crystal plane, and catalytic activity of Co$_3$O$_4$ to activate MPS for phenol degradation. Thus, the aim of this study is to elucidate how different morphologies of Co$_3$O$_4$ catalysts with various well-defined planes (i.e., dominant exposed facets) would affect their characteristics and catalytic activities for MPS activation to degrade phenol. Specifically, three Co$_3$O$_4$ nanocrystals are fabricated to exhibit morphologies of nanoplate (NP), nanobundle (NB), and nanocube (NC) (as shown in Fig. 1(a)), and

three Co_3O_4 nanocrystals are characterized to distinguish their dominant exposed facets, and physical/chemical properties, which, in turn, influence their catalytic activities towards MPS activation and phenol degradation.

2. Experimental

All chemical reagents in this study were of analytical grade and used directly without purification. Three Co_3O_4 nanocrystals were prepared via hydrothermal processes under different conditions to afford Co_3O_4-NP, Co_3O_4-NB, and Co_3O_4-NC. The detailed preparation methods and materials characterizations can be found in the supporting information (Text S1). In addition, detailed procedures for phenol degradation using various Co_3O_4 nanocrystals, and MPS can be also found in the supporting information.

3. Results and Discussion

3.1 Characterization of various Co_3O_4 nanocrystals

Morphologies of the as-prepared Co_3O_4 nanocrystals were visualized firstly by SEM. In general, morphology of nanostructures can be manipulated through anisotropic growth of the self-aggregation process of crystallites [32]. Thus, shapes of Co_3O_4 can be varied via influencing their formations of small crystalline nuclei by adding additives (e.g., directing agents, surfactants, and soft templates), and using different cobaltic salts [32, 33]. As different cobaltic salts and directing agents were employed in this study, various shapes of Co_3O_4 nanocrystals can be therefore obtained here. For instance, hexamethylenetetramine was employed here for preparing Co_3O_4-NP as hexamethylenetetramine is a strong chelating ligand and has been unveiled as a molecular building block for self-assembled molecular crystals, facilitating the growth

of sheet-like morphology [9]. In the case of Co_3O_4-NB, ethylene glycol was particularly used as ethylene glycol serves as a rate-controlling agent, producing a rod-like precursor of cobalt hydroxide carbonate [10]. On the other hand, an oxidant, H_2O_2, was particularly added in the case of Co_3O_4-NC as H_2O_2 would oxidize Co^{2+} into Co^{3+}, anions in solutions would be then intercalated into the inter-layered space to compensate the extra positional charge inferred by Co^{3+} cations, resulting the nanoscale cubic morphology [11].
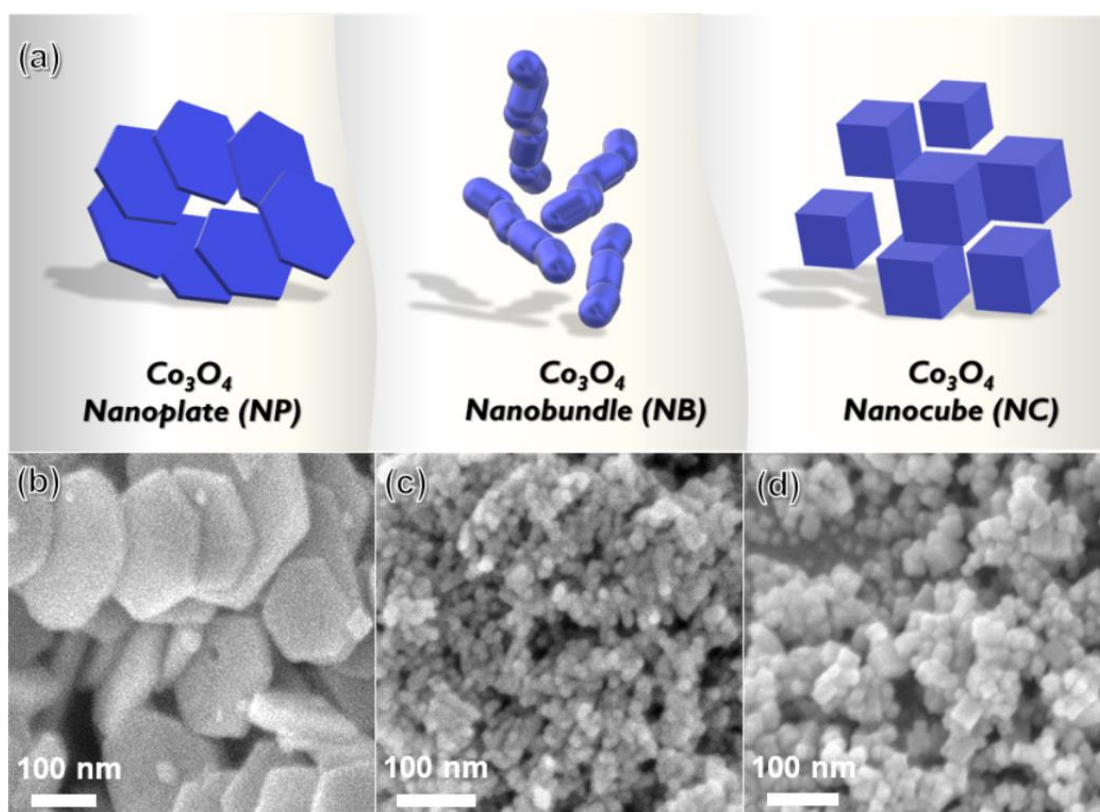

Fig. 1. Various Co_3O_4 nanocrystals: (a) illustrations and (b-d) SEM images.

Fig. 1(b) shows that the resultant Co_3O_4-NPs certainly exhibited the plate-like morphology with a special hexagonal shape. Size of these plates were in the range of 100~300 nm, validating the nanoscale dimension of these plates. Its TEM image (Fig. 2(a)) also ascertained that these plates were very thin, and its hexagonal shape can be well-defined. Next, the morphology of the resultant Co_3O_4-NB can be seen in Fig. 1(c), in which many rounded particles (with sizes of 20 ~ 40 nm) were agglomerated to bundle together. Its corresponding TEM image (Fig. 2(b)) also confirmed that these rounded particles were connected to form nanobundles. On the other hand, Fig. 1(d) shows the SEM image of Co_3O_4-NC, in which many small cubes can be easily observed. The TEM image (Fig. 2(c)) also revealed that the cubic shape of these Co_3O_4-NCs were well-defined, and their sizes were in the range of 20 ~ 40 nm, confirming the successful formation of nanocube in Co_3O_4-NC.
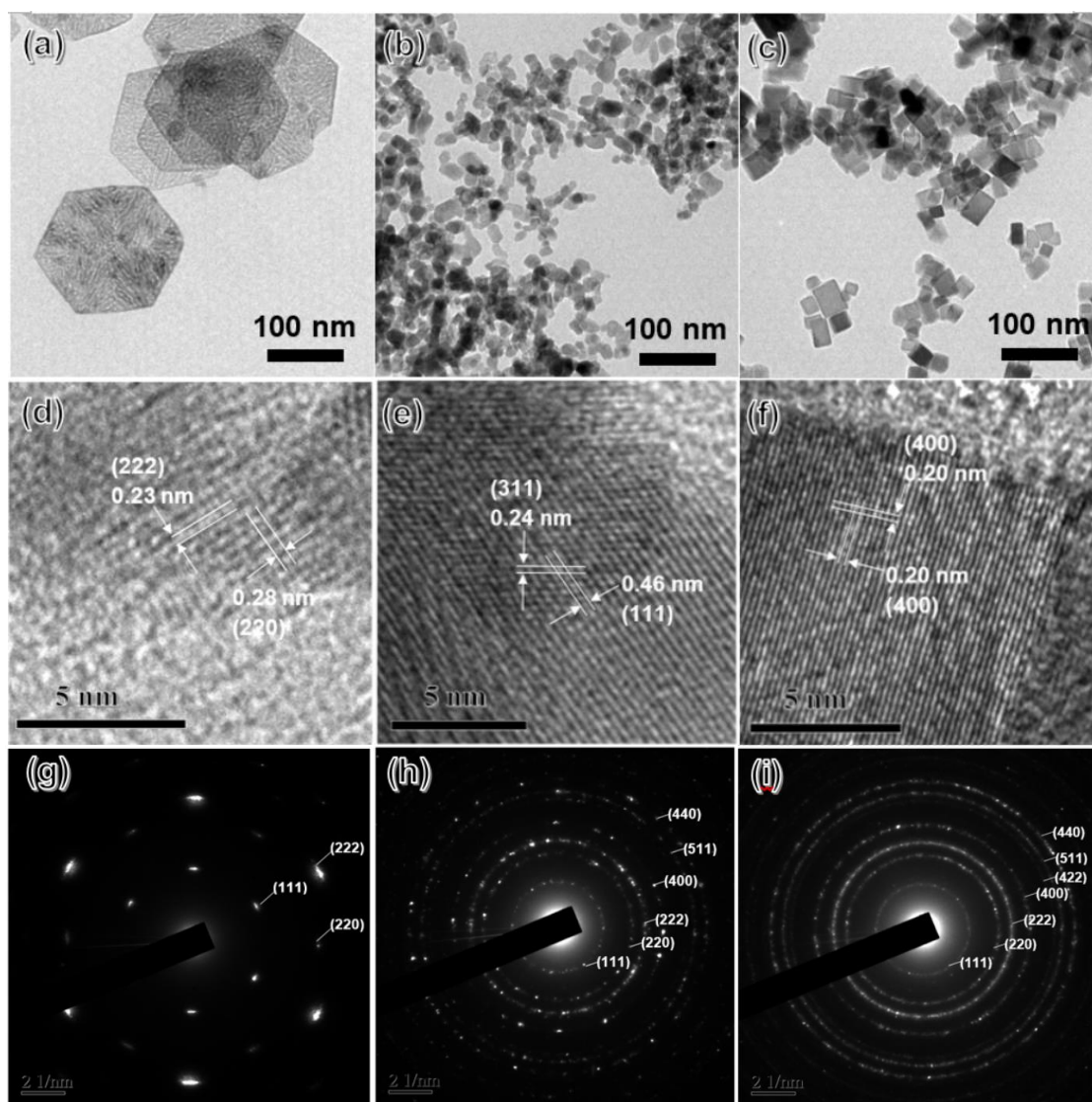
Fig. 2. (a-c) TEM images, (d-f) HRTEM images, and (g-i) SAED patterns of Co$_3$O$_4$-NP, Co$_3$O$_4$-NB, and Co$_3$O$_4$-NC nanocrystals, respectively.

Moreover, lattice-resolved HRTEM, and selected area electron diffractions (SAED) of these three Co$_3$O$_4$ nanocrystals were characterized to further identify their crystalline structural information. Fig. 2(d) displays the lattice-resolved HRTEM image of Co$_3$O$_4$-NP, in which (220), and (222) crystal planes of Co$_3$O$_4$ with d-spacing of 0.28 and 0.23 nm, respectively, can be detected. This confirms that the resultant Co$_3$O$_4$-NP was certainly comprised of Co$_3$O$_4$, and its main exposed facet was {112}. On the other hand, its corresponding SAED (Fig. 2(g)) also ascertained that Co$_3$O$_4$-NP exhibited a well-defined polycrystalline structure [34, 35]. Next, Fig. 2(e) displays a HRTEM

8

image of Co$_3$O$_4$-NB, in which (311), and (111) crystal planes of Co$_3$O$_4$ with *d*-spacing

of 0.24 and 0.46 nm, respectively, can be found, indicating that Co$_3$O$_4$-NB exhibited a

main exposed facet of {110}. Its SAED (Fig. 2(h)) also validated that Co$_3$O$_4$-NB

possessed the well-developed poly-crystalline structure. In addition, Fig. 2(f) displays

a HRTEM image of Co$_3$O$_4$-NC, in which only the (400) crystal plane of Co$_3$O$_4$ with a

d-spacing of 0.200 nm can be observed, suggesting that the main exposed facet of

Co$_3$O$_4$-NC was {100}. The corresponding SAED also validated that Co$_3$O$_4$-NC

possessed the well-developed polycrystalline structures.

While the SAED analyses of these Co$_3$O$_4$ nanocrystals had suggested

polycrystalline natures of Co$_3$O$_4$, their XRD patterns were additionally determined in

Fig. 3(a), in which noticeable peaks at 19.0°, 31.3°, 36.8°, 38.5°, 44.8°, 59.4° and 65.2°

can be detected, and attributed to the (111), (220), (311), (222), (400), (422), (511),

(440) and (533) planes of Co$_3$O$_4$ according to JCPDS #42-1467.
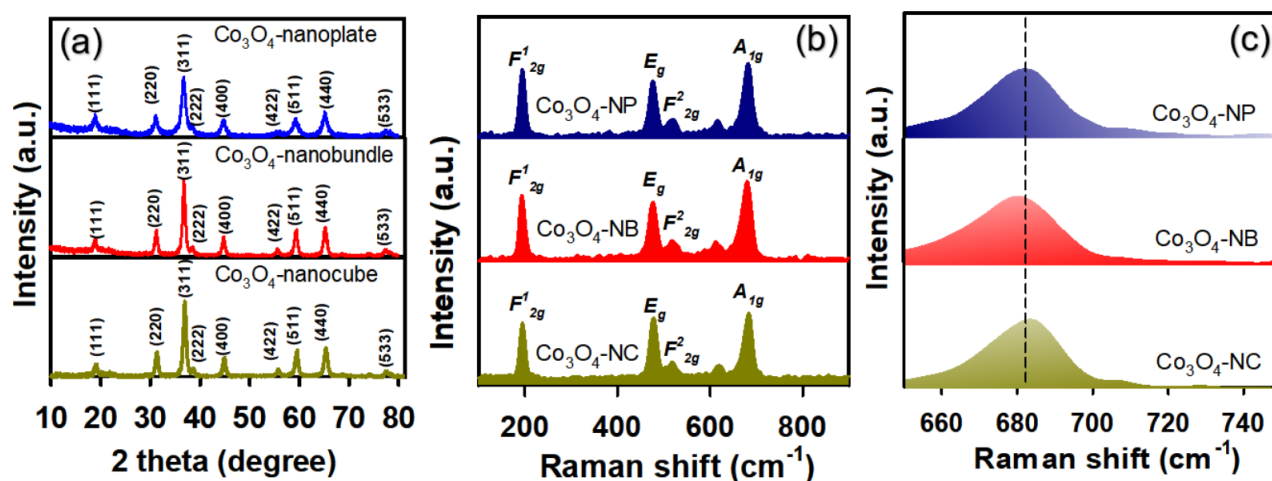

Fig. 3. (a) XRD, (b) Raman spectra, and (c) regional Raman spectra of various Co$_3$O$_4$ nanocrystals.

Moreover, Raman spectroscopic analyses of these Co_3O_4 nanocrystals were also obtained in Fig. 3(b), in which several signature peaks of Co_3O_4 can be observed in the region of 190~700 Raman shift (cm^{-1}). The peaks at 195, 525, and 620 cm^{-1} were ascribed to the F_{2g} symmetry of Co_3O_4 [36], whereas the peak at 485 cm^{-1} corresponded to the E_g symmetry. Besides, the peak at 695 cm^{-1} could be assigned for the A_{1g} symmetry of Co_3O_4 [37, 38]. Moreover, a further comparison of the A_{1g} peak (at *ca.* 695 cm^{-1}) was additionally displayed in Fig. 3(c), and their peak centers were noticeably differentiated. For instance, the A_{1g} peak center of Co_3O_4-NB moved towards the lower frequency with respect to that of Co_3O_4-NP, whereas the A_{1g} peak center of Co_3O_4-NC shifted towards the higher frequency. As the A_{1g} peak of Co_3O_4 is associated with structural defection [36], peak shifts towards lower frequencies suggest more structural defections. Such a comparison indicated that these three Co_3O_4 nanocrystals with different morphologies and main exposed facets would also exhibit slightly different structural defection, which might influence their catalytic activities [39].

Furthermore, surface chemistries of these Co_3O_4 nanocrystals were analyzed by XPS, and their Co2p and O1s XPS spectra are displayed in Fig. 4(a), and (b), respectively. All of these Co_3O_4 nanocrystals showed similar Co2p spectra, which were then deconvoluted to reveal a series of underlying peaks in the range of 775-810 eV. Specifically, the peaks at 780.2 and 795.1 eV could be ascribed to Co^{3+}, whereas the peaks at 781.8 and 796.9 eV corresponded to Co^{2+}, confirming the existence of Co_3O_4 in these nanocrystals [40].
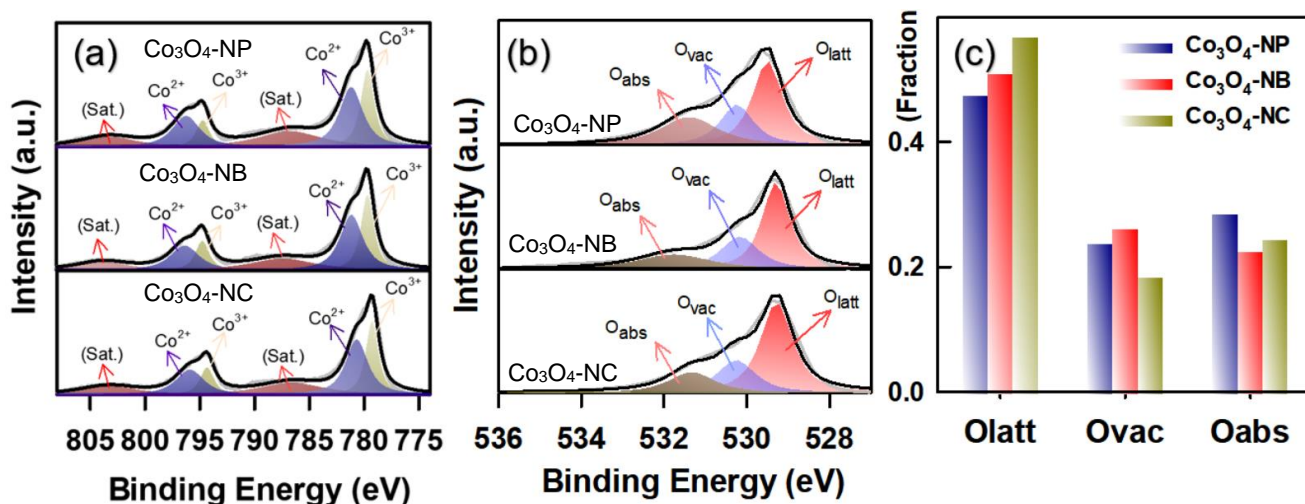
Fig. 4. XPS analyses of various Co_3O_4 nanocrystals: (a) Co2p, (b) O1s, and (c) fractions of O species.

In addition, the O1s spectra of these Co_3O_4 nanocrystals can be also deconvoluted to exhibit three underlying peaks at 529.7, 531.1, and 532.0 eV, which were attributed to the lattice oxygen (O_{latt}), oxygen vacancy (O_{vac}) and absorbed oxygen (O_{abs}), respectively [41, 42]. As O_{vac} is associated with catalytic activities of Co_3O_4 [43, 44], fractions of O_{vac} in these Co_3O_4 nanocrystals were then compared in Fig. 4(c), and Co_3O_4-NB exhibited a relatively high fraction of O_{vac}, followed by Co_3O_4-NP, and Co_3O_4-NC. Since Ovac can be also related to structural defection [43], such an order of Ovac fractions in these Co_3O_4 nanocrystals was in line with the aforementioned Raman spectroscopic analysis, in which Co_3O_4-NB seemed to show more structural defection, followed by Co_3O_4-NP, and Co_3O_4-NC.

In addition, temperature-programmed reduction (TPR) analyses of these Co_3O_4 nanocrystals were also conducted as shown in Fig. 5(a), and the TPR profiles of these Co_3O_4 nanocrystals can be essentially ascribed to two stages. The first stage at around 300 °C can be attributed to the reduction of Co^{3+} to Co^{2+}, whereas the second stage at > 400 °C can be assigned to the reduction of Co^{2+} to Co^0 [36, 45]. Nevertheless, the center of the first reduction stage in Co_3O_4-NB seemed to occur at a much lower

temperature than those of Co_3O_4-NP, and Co_3O_4-NC. This result suggested that the surficial catalytic activities of these Co_3O_4 nanocrystals were quite different owing to their distinct characteristics as discussed in the earlier section.
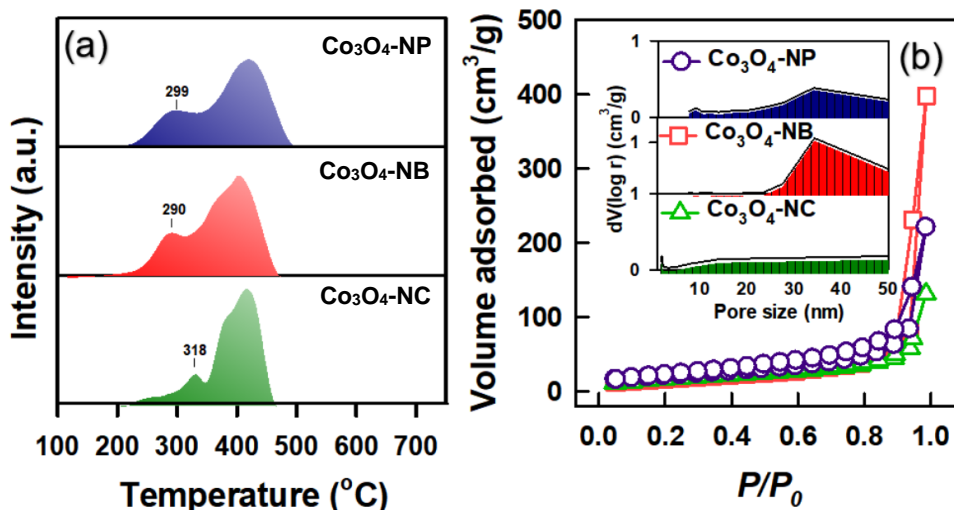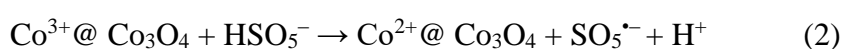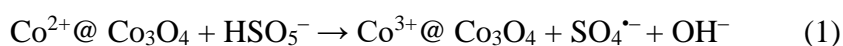

Fig. 5. (a) TPR profiles, and (b) N_2 sorption isotherms (the inset is the pore size distribution) of various Co_3O_4 nanocrystals.

As these Co_3O_4 nanocrystals showed different morphologies, their textural properties were then also investigated. Firstly, N_2 sorption isotherms of these Co_3O_4 nanocrystals were measured in Fig. 5(b). Their N_2 sorption amounts were quite comparable, and all these N_2 sorption isotherms could be regarded as the IUPAC type III isotherm. Their corresponding surface areas for Co_3O_4-NP, Co_3O_4-NB, Co_3O_4-NC were 75.5, 57.4, and 60.6 m^2/g, respectively. On the other hand, their corresponding pore size distributions can be seen in Fig. 5(b). Essentially, all these Co_3O_4 nanocrystals possessed mesopores, and pore volumes of Co_3O_4-NP, Co_3O_4-NB, Co_3O_4-NC were 0.33, 0.60, and 0.20 m^2/g, respectively. The relatively high pore volume in Co_3O_4-NB could be attributed to small voids between the rounded particles.

3.2 Degradation of phenol using MPS activated by Co₃O₄ nanocrystals

For evaluating phenol degradation using MPS activated by these Co_3O_4 nanocrystals, it would be also necessary to examine whether phenol would be adsorbed to these Co_3O_4 nanocrystals. Fig. 6(a) reveals phenol could be slightly removed in the presence of these Co_3O_4 nanocrystals as their corresponding C_t/C_0 of phenol approached ~0.95 after 120 min. This indicated that phenol could not be eliminated effectively simply via adsorption to these Co_3O_4 nanocrystals. On the other hand, MPS alone was also investigated for degrading phenol but MPS in the absence of any activators was almost useless for phenol degradation. However, once MPS combined with these Co_3O_4 nanocrystals, phenol could be rapidly degraded, and fully eliminated by all these Co_3O_4 nanocrystals within 120 min. These results indicate that MPS could be activated by these Co_3O_4 nanocrystals to degrade phenol.

Since these Co_3O_4 nanocrystals comprised of Co^{2+}, and Co^{3+}, these cobalt species could react with MPS to convert MPS anions (HSO_5^-) into sulfate and MPS radicals as follows (Eqs.(1)-(2)) [18]:

$$Co^{2+}@ \ Co_3O_4 + HSO_5^- \rightarrow Co^{3+}@ \ Co_3O_4 + SO_4^{\bullet-} + OH^- \qquad (1)$$

$$Co^{3+}@ \ Co_3O_4 + HSO_5^- \rightarrow Co^{2+}@ \ Co_3O_4 + SO_5^{\bullet-} + H^+ \qquad (2)$$

$SO_5^{\bullet-}$ would be further transformed into a sulfate radical through its self-dissociation (Eq.(3)):

$$2 \ SO_5^{\bullet-} \rightarrow 2 \ SO_4^{\bullet-} + O_2 \qquad (3)$$

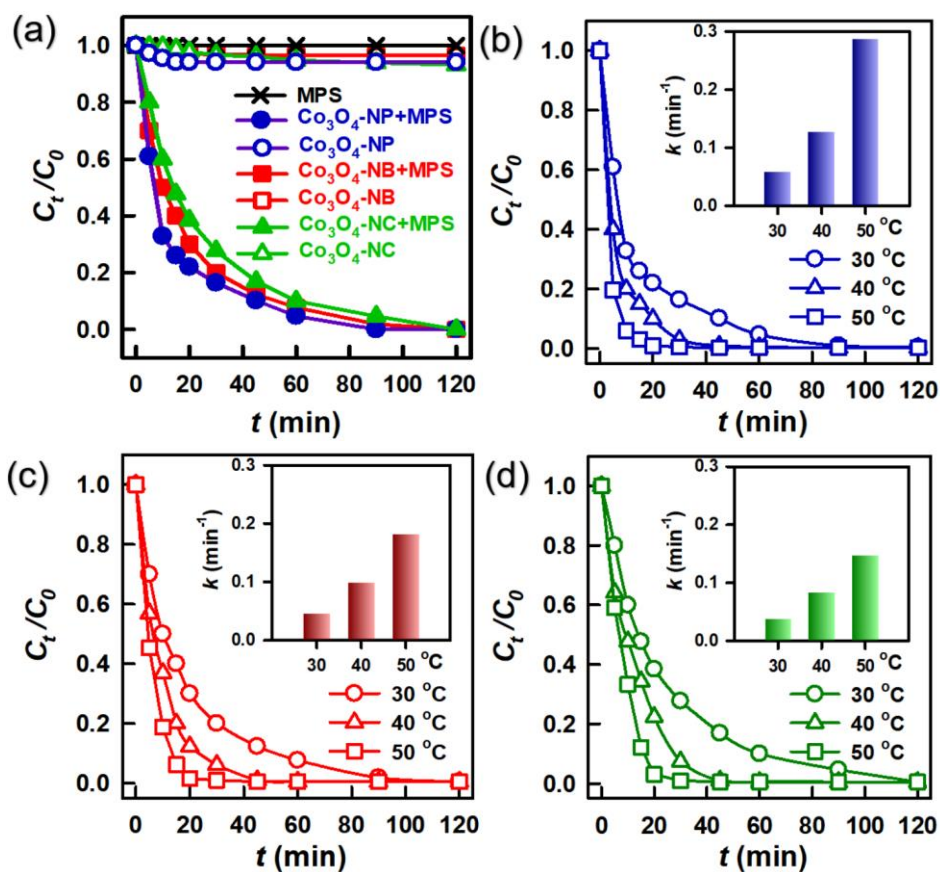These resulting sulfate radicals would then decompose phenol, and cause degradation.

Fig. 6. (a) Comparisons for degradation of phenol by various Co_3O_4 nanocrystals at 30 °C; effect of temperature on phenol degradation by (b) Co_3O_4-NP, (c) Co_3O_4-NB, and (d) Co_3O_4-NC (catalyst = 150 mg/L, MPS = 200 mg/L, and phenol = 5 mg/L).

While these Co_3O_4 nanocrystals all successfully activated MPS to degrade phenol, their degradation behaviors seemed slightly different in terms of degradation kinetics. For quantifying degradation kinetics, the pseudo first order model $C_t = C_0 e^{-kt}$, which has been widely adopted to calculate rate constants (k) of MPS-involved degradation, was then applied here. The k of phenol degradation by Co_3O_4-NP/MPS was calculated as 0.061 min^{-1}, 0.047 min^{-1} for Co_3O_4-NB/MPS, and 0.040 min^{-1} for Co_3O_4-NC/MPS, respectively. This suggests that even though these Co_3O_4 nanocrystals consisted of the same composition, their catalytic activities seemed slightly different as their physical

and chemical characteristics were quite distinct as discussed in the earlier section. In particular, the catalytic activity of Co_3O_4-NP appeared to be slightly higher. This was possibly because Co_3O_4-NP exhibited a noticeably higher surface area than other two Co_3O_4 nanocrystals, and a higher surface area offered more reactive surfaces for activating MPS. On the other hand, dominant exposed facets of metal oxides also substantially affect their catalytic activities [39, 46-48]. As Co_3O_4-NP had the dominant exposed facet of {112}, this plane comprises of two Co^{2+} ions and two Co^{3+} ions on its surface layer according to its surface atomic configuration (Fig. S1) [46, 49, 50]. In contrast, Co_3O_4-NC with the main exposed plane {100}

would comprise only a Co^{2+} ion, and no Co^{3+} ion on its surface layer. Therefore, the activation process of MPS by Co_3O_4-NP would be slightly different from that by Co_3O_4-NC, and a faster and more effective activation process can be expected by using Co_3O_4-NP. Thus, the phenol degradation proceeded faster in the case of Co_3O_4-NP/MPS.

Additionally, while the {110} plane as observed in Co_3O_4-NB consists a similar configuration (i.e., two Co^{2+} ions and two Co^{3+} ions) as Co_3O_4-NP on its surface layer, the high-index {112} plane in Co_3O_4-NP is expected to contain more open structures than the {110}, enabling Co_3O_4-NP still to exhibit a higher-degree catalytic activity then Co_3O_4-NB. Moreover, even though Co_3O_4-NB seemed to possess a slightly more structural defection, the relatively low surface area of Co_3O_4-NB might make the activation process less effective, thereby leading to the slower kinetics. In view of these results, the surface area appeared as the most dominant factor among various physical and chemical parameters to determine catalytic activities of these Co_3O_4 nanocrystals.

Moreover, a commercial Co_3O_4 nanoparticle was also tested, and the result is added to the supporting information (Fig. S2). While the commercial Co_3O_4 was able to activate MPS to degrade phenol, its catalytic activity was apparently much lower

than the proposed Co_3O_4 nanostructures here. A possible reason was because the surface area of the commercial Co_3O_4 nanoparticle was ≤ 10 m^2/g, much lower than those of the proposed nanostructures, leading to the much more inefficient degradation. This result also suggests that the surface area seemed to play a dominant role in catalytic activities of Co_3O_4 for activating MPS to degrade phenol.

3.3 Effect of temperature on phenol degradation by Co_3O_4/MPS

As temperature represents an important parameter for degradation of pollutants using MPS, the effect of temperature on phenol degradation using MPS activated by these Co_3O_4 nanocrystals was then investigated. Fig. 6(b) shows phenol degradation by Co_3O_4-NP/MPS at 30, 40, and 50 °C. At these three temperatures, phenol was all fully eliminated in 120 min. Nevertheless, the degradation kinetics was considerably varied at different temperatures, and thus the corresponding rate constants were calculated as 0.061 min^{-1} at 30 °C, 0.128 min^{-1} at 40 °C, and 0.286 min^{-1} at 50 °C (the inset of Fig. 6(b)), respectively, demonstrating that a higher temperature certainly accelerated phenol degradation by Co_3O_4-NP/MPS.

Similar results can be observed in the cases of phenol degradation by Co_3O_4-NB/MPS and Co_3O_4-NC/MPS as rate constants were substantially increased at elevated temperatures. For instance, k obtained by Co_3O_4-NB/MPS at 30 was 0.047 min^{-1} at 30 °C, 0.128 min^{-1} at 40 °C, and 0.286 min^{-1} at 50 °C, respectively, whereas, k obtained by Co_3O_4-NB/MPS was 0.040 min^{-1} at 30 °C, 0.085 min^{-1} at 40 °C, and 0.1475 min^{-1} at 50 °C, respectively. These results confirmed that the increase in temperature would enhance phenol degradation by Co_3O_4/MPS. However, the enhancement in the case of Co_3O_4-NP/MPS was much more noticeable than those seen in the cases of Co_3O_4-NB/MPS and Co_3O_4-NC/MPS. This suggests that Co_3O_4-NP exhibited a higher

catalytic activity than the other two Co_3O_4 nanocrystals not only at ambient temperature but also at elevated temperatures.

3.4 Effect of pH on phenol degradation by Co_3O_4/MPS

Furthermore, since MPS activation, and phenol degradation both occur in water, pH is also one of the most important parameters, and thus it was investigated by changing pH value of phenol solution to 3, 5, 7, 9, and 11. Fig. 7(a) shows phenol degradation by Co_3O_4-NP/MPS at different pH values. When the phenol solution became slightly acidic at pH = 5, the corresponding phenol degradation was noticeably influenced as phenol could not be fully eliminated in 120 min as the C_t/C_0 was merely 0.11. As the phenol solution became even more acidic at pH = 3, the adverse effect on phenol degradation was intensified as the corresponding C_t/C_0 was 0.15 at 120 min.
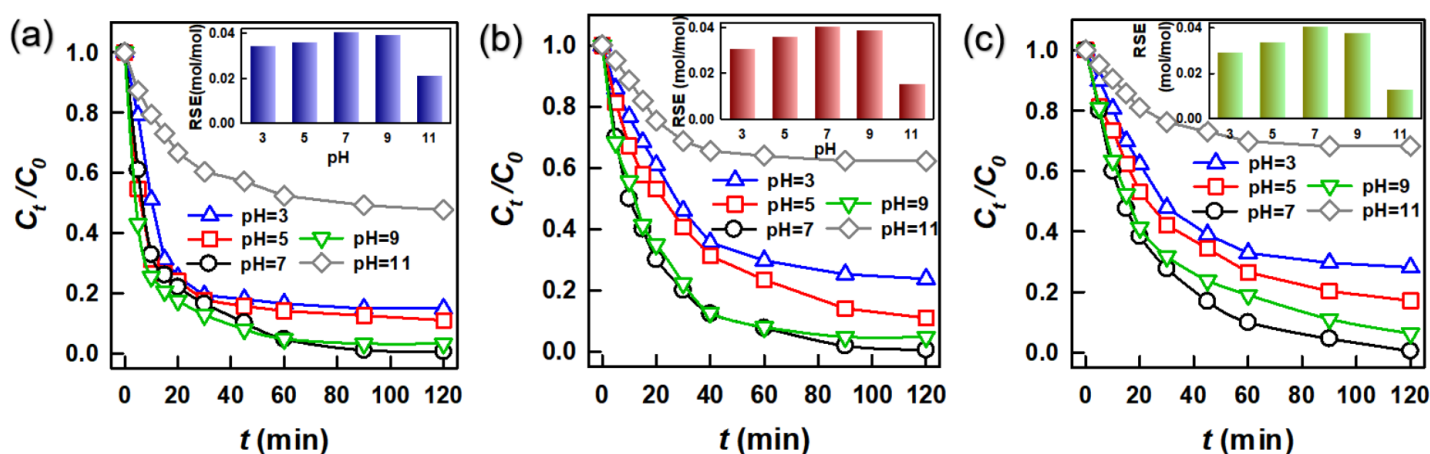

Fig. 7. Effect of pH on phenol degradation by (a) Co_3O_4-NP, (b) Co_3O_4-NB, and (c) Co_3O_4-NC at 30 °C (catalyst = 150 mg/L, MPS = 200 mg/L, and phenol = 5 mg/L).

These results suggested that varying initial pH value certainly altered catalytic activities, thereby influencing degradation efficiencies. To further quantify degradation efficiencies by Co_3O_4-NP/MPS under various conditions, their reaction stoichiometric efficiencies (RSE) were then calculated as RSE has increasingly adopted to quantify catalytic activity for activating MPS by catalysts via the following equation (Eq. 4) [51]:

$$Reaction\ Stoichiometric\ Efficiency\ \left(RSE\right)\ = \frac{\text{phenol degraded (mole)}}{\text{MPS added (mole)}} \quad (4)$$

As displayed in the inset of Fig. 7(a), RSE at pH = 7 by Co_3O_4-NP/MPS was 0.040, which decreased to 0.036 at pH = 5, and then 0.34 at pH = 3, confirming that the acidic condition was unfavorable to phenol degradation by Co_3O_4-NP/MPS. This was possibly because MPS tends to be more stable in acidic environments and therefore becomes more difficult to be activated for production of radicals [28]. On the other hand, when the phenol solution became slightly basic at pH = 9, interestingly the phenol degradation was not considerably influenced as the corresponding RSE was 0.039, very close to that at pH = 7. Nevertheless, when the solution became more basic at pH = 11, the degradation behavior was tremendously affected as the RSE was substantially decresed to 0.021. Such a negative effect of basic conditions was attributed to the fact that MPS would decompose without production of $SO_4^{\bullet-}$ in basic environments [52] and therefore $SO_4^{\bullet-}$ was not efficiency produced to degrade phenol. Furthermore, as the pKa of HSO_5^- was 9.4 [53], HSO_5^- could be possibly transformed into HSO_5^- under basic conditions and thus the electrostatic revulsion might also become stronger, refraining the approach of SO_5^{2-} towards Co_3O_4-NP, and hindering phenol degradation.

Similar effects of pH variation on phenol degradation can be also observed in the cases of phenol degradation by Co_3O_4-NB/MPS and Co_3O_4-NC/MPS as the acidic conditions would noticeably influenced phenol degradation behaviors by decreasing

RSE. Besides, the highly basic conditions would cause phenol degradation to be ineffective with very low RSE values, whereas phenol degradation was not notably altered under the slightly basic condition (i.e., pH = 9). Nevertheless, an interesting feature can be observed that even though pH variation certainly influenced phenol degradation by these Co_3O_4 nanocrystals with MPS, the influence on phenol degradation by Co_3O_4-NP/MPS seemed much less pronounced especially at pH = 3 to 9. This also demonstrated that Co_3O_4-NP appeared to be more resistant than the other two Co_3O_4 nanocrystals. These investigations also validated advantages of Co_3O_4-NP over the other two Co_3O_4 nanocrystals.

3.5 The mechanism of phenol degradation by Co_3O_4/MPS

The earlier sections certainly validated that these Co_3O_4 nanocrystals Co_3O_4 were certainly capable of activating MPS to degrade phenol. Even though activation of MPS typically generates $SO_4^{\bullet-}$, $SO_4^{\bullet-}$ in water might further evolve into $^{\bullet}OH$ via the following reaction: $SO_4^{\bullet-} + H_2O \rightarrow SO_4^{2-} + {}^{\bullet}OH + H^+$. Thus, it would be necessary to elucidate whether $SO_4^{\bullet-}$ and $^{\bullet}OH$ both contributed to phenol degradation using these Co_3O_4 nanocrystals with MPS. To this end, two radical scavengers, TBA, and methanol, were particularly selected as TBA has been extensively adopted as a probe indicator for $^{\bullet}OH$ because TBA can quickly react with $^{\bullet}OH$ because of no α-hydrogen in TBA, whereas methanol can rapidly react both with $SO_4^{\bullet-}$ and $^{\bullet}OH$.

Firstly, Fig. 8(a) shows that phenol degradation in the presence of TBA was notably influenced as its corresponding RSE decreased from 0.040 (obtained in the absence of any scavengers) to 0.033, suggesting that $^{\bullet}OH$ might exist and contribute to phenol degradation in the case of Co_3O_4-NP/MPS. Furthermore, when methanol was

added, the RSE dropped significantly to 0.007, indicating that both $SO_4^{\bullet-}$ and $^\bullet OH$ occurred from Co_3O_4-NP/MPS and contributed together to phenol degradation.

Similar results can be also observed in the cases of Co_3O_4-NB/MPS, and Co_3O_4-NC/MPS in Fig. 8(b-c), showing that the presence of TBA slightly hindered phenol degradation but the addition of methanol tremendously inhibited phenol degradation by using these two Co_3O_4 nanocrystals. This also indicated that $^\bullet OH$ was possibly derived from $SO_4^{\bullet-}$ to contribute jointly to phenol degradation.
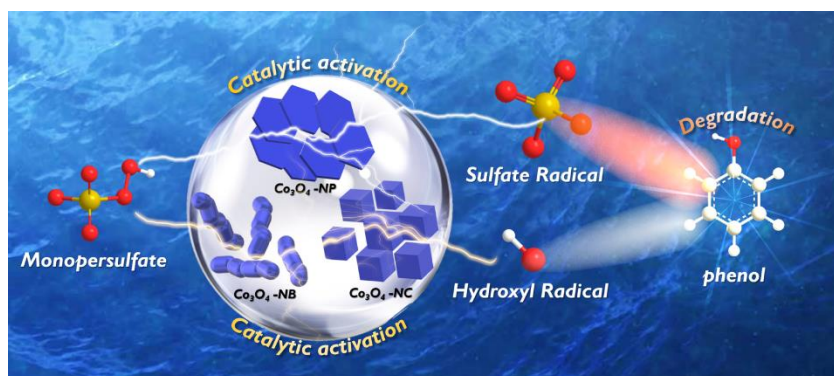

(e)
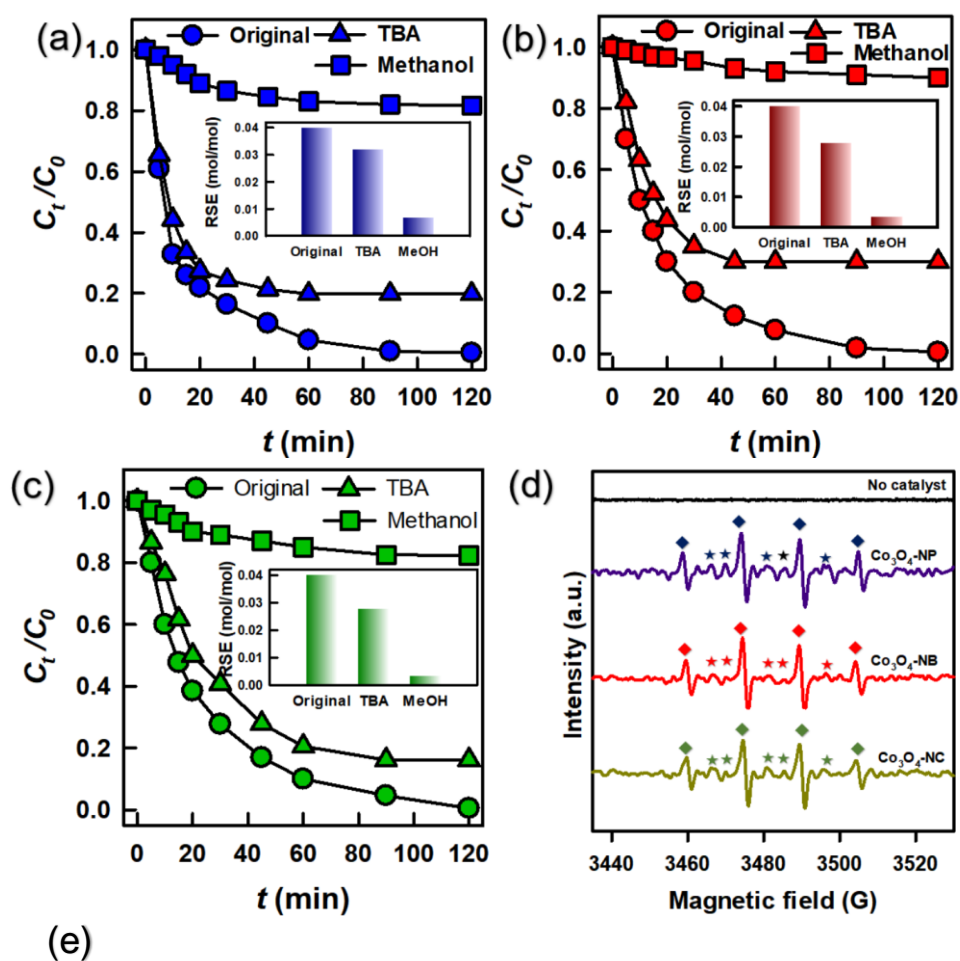
Fig. 8. Effect of scavengers on phenol degradation by (a) Co_3O_4-NP, (b) Co_3O_4-NB, and (c) Co_3O_4-NC at 30 °C (catalyst = 150 mg/L, MPS = 200 mg/L, and phenol = 5 mg/L); (d) EPR analyses of MPS activation by various 3D Co_3O_4 nanocrystal (★: DMPO-SO$_4$; ◆: DMPO-OH) ; and (e) the proposed mechanism of phenol degradation by these Co_3O_4 nanocrystals and MPS.

For further identifying radical species generated from these Co_3O_4 nanocrystals with MPS, electron paramagnetic resonance (EPR) analysis was adopted by using DMPO as the spin-trapping agent in Fig. 8(d). As almost no noticeable pattern can be detected in the case of MPS, noticeable and similar patterns can be observed as these Co_3O_4 nanocrystals and MPS were both present. Such a pattern can be ascribed to the hyperfine splitting of oxidation adduct products of DMPO-SO$_4$ and DMPO-OH [54], validating that both $SO_4^{\bullet-}$ and $^{\bullet}OH$ were assuredly generated from MPS activation by these Co_3O_4 nanocrystals, contributing phenol degradation as illustrated in Fig. 8(e).

3.6 The recyclability of Co_3O_4 nanocrystals to activate MPS for phenol degradation

Although these Co_3O_4 nanocrystals were validated to activate MPS, it would be also imperative to verify whether these Co_3O_4 nanocrystals can be reused for activating MPS. Fig. 9(a) firstly shows the multi-cycle phenol degradation by Co_3O_4-NP/MPS, and phenol could be continuously and effectively eliminated by the spent Co_3O_4-NP, showing that Co_3O_4-NP could be recyclable and its catalytic activity remained durable and effective. On the other hand, Co_3O_4-NB and Co_3O_4-NC could be also re-used to activate MPS for degrading phenol as seen in Fig. 9(b-c). Nevertheless, slight variations in degradation efficiencies can be observed when these nanocrystals were continuously reused over many cycles. This was possibly because these nanocrystals did not receive any regeneration and cleansing treatments during the recyclability test, and some intermediates might be deposited onto surfaces of these Co_3O_4 nanocrystals, hindering phenol degradation slightly.
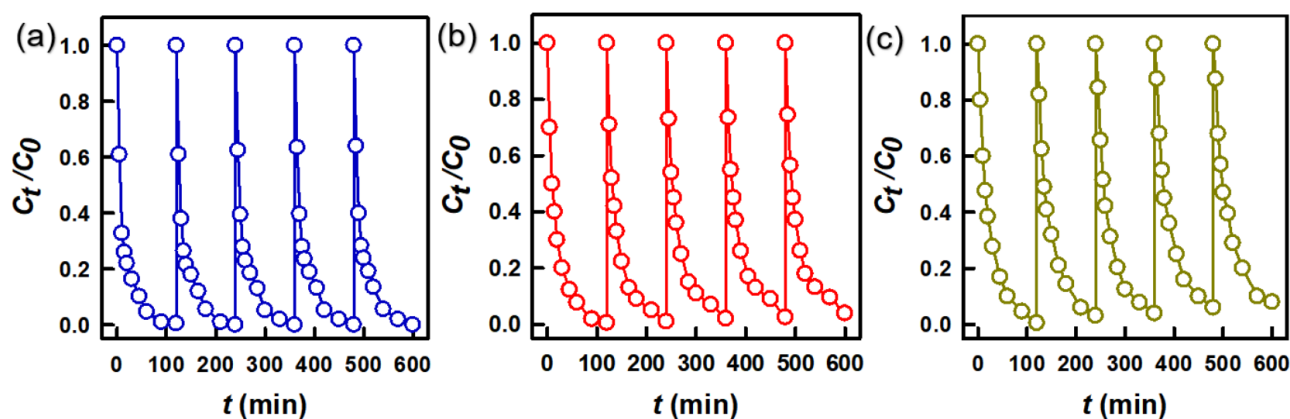
Fig. 9. Recyclability of (a) Co_3O_4-NP, (b) Co_3O_4-NB, and (c) Co_3O_4-NC for phenol degradation at 30 °C (catalyst = 150 mg/L, MPS = 200 mg/L, and phenol = 5 mg/L).

3.7 A potential phenol degradation pathway for by Co_3O_4-NP/MPS

As Co_3O_4-NP was validated to exhibit higher, more resistant, and more durable catalytic activity for activating MPS to degrade phenol, it would be useful to investigate

phenol degradation pathway by Co_3O_4-NP/MPS. Therefore, degradation by-products of phenol were then identified by mass spectrometry and listed in Table S1. According to these degradation by-products, a possible degradation pathway of phenol by Co_3O_4-NP/MPS could be proposed in Fig. 10.

In the beginning, phenol would be oxidized and inserted with a hydroxyl group to form C1 (Pyrocatechol/hydroquinone), which would be then further oxidized to afford C2 (benzoquinone). After benzoquinone was attacked and undergone a ring-opening reaction, benzoquinone would be transformed to C3 (maleic acid), which could be then decomposed to generate many smaller molecules, such as C4 (oxalic acid). Through continuous oxidation, oxalic acid could be then decomposed into C5 (2-hydroxyacetic acid), and then C5 (carbonic acid). These low-molecular-weight compounds would be further oxidized and eventually become CO_2 and H_2O.
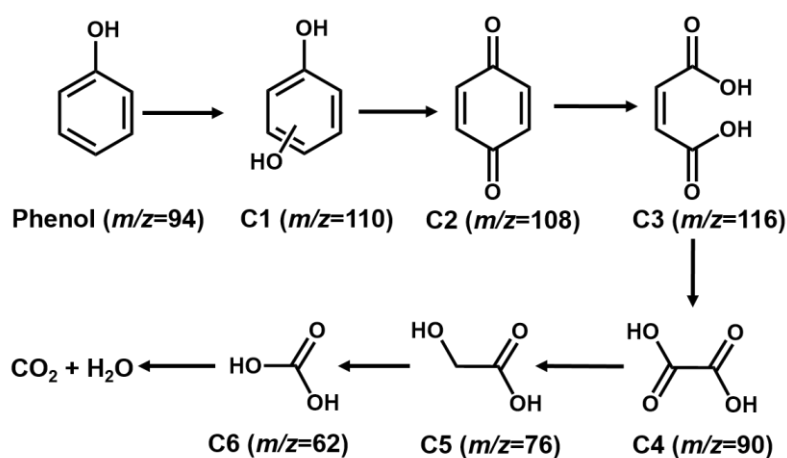

Fig. 10. A potential degradation pathway of phenol by Co_3O_4-NP and MPS.

4   Conclusions

In this study, three Co_3O_4 nanocrystals with very distinct morphologies, and, more importantly, different main exposed facets were particularly prepared and compared in order to probe into the morphology-property-catalytic activity relationship of Co_3O_4 for

activating MPS to degrade a ubiquitous persistent pollutant, phenol. Through adopting different additives and cobaltic precursors, Co_3O_4-NP, Co_3O_4-NB, and Co_3O_4-NC were fabricated, and characterized. While these three Co_3O_4 nanocrystals were all comprised of Co_3O_4, Co_3O_4-NP, Co_3O_4-NB, and Co_3O_4-NC possessed different dominant exposed facets of {112}, {110}, and {100}, respectively. As the facets of {112} and {110} consisted of more abundant Co^{2+} and Co^{3+} ions on their surfaces, Co_3O_4-NP and $Co3O4$-NB exhibited noticeably higher catalytic activities then Co_3O_4-NC for activating MPS to degrade phenol. Nevertheless, since Co_3O_4-NP showed a much higher surface area than Co_3O_4-NB, Co_3O_4-NP could exhibit a relatively high catalytic activity in comparison to Co_3O_4-NB. In addition, Co_3O_4-NP also exhibited much faster degradation kinetics, more resistance towards influence of pH variation and higher recyclability than the other two Co_3O_4 nanocrystals. These features made Co_3O_4-NP a more outstanding Co_3O_4 for activating MPS to degrade phenol. The mechanism of phenol degradation using MPS activated by Co_3O_4-NP as well as other Co_3O_4 nanocrystals was also elucidated and attributed to both $SO_4^{\bullet-}$ and $^\bullet OH$. Furthermore, the phenol degradation pathway by Co_3O_4-NP/MPS was also investigated and proposed. These findings revealed that Co_3O_4 nanocrystals can be manipulated to enhance its catalytic activity for activating MPS through varying morphologies, and main exposed facets.

References:

1. Rocha, L.L., et al., *Isolation and characterization of phenol-degrading yeasts from an oil refinery wastewater in Brazil.* Mycopathologia, 2007. **164**(4): p. 183-188.
2. Lazarova, Z. and S. Boyadzhieva, *Treatment of phenol-containing aqueous solutions by membrane-based solvent extraction in coupled ultrafiltration modules.* Chemical Engineering Journal, 2004. **100**(1): p. 129-138.

3.	Li, K., et al., *Fabrication of H3PW12O40-doped carbon nitride nanotubes by one-step hydrothermal treatment strategy and their efficient visible-light photocatalytic activity toward representative aqueous persistent organic pollutants degradation.* Applied Catalysis B: Environmental, 2014. **156-157**: p. 141-152.

4.	Carmona, M., et al., *Combined adsorption and ion exchange equilibrium of phenol on Amberlite IRA-420.* Chemical Engineering Journal, 2006. **117**(2): p. 155-160.

5.	Padhi, D.K., et al., *Green Synthesis of Fe3O4/RGO Nanocomposite with Enhanced Photocatalytic Performance for Cr(VI) Reduction, Phenol Degradation, and Antibacterial Activity.* ACS Sustainable Chemistry & Engineering, 2017. **5**(11): p. 10551-10562.

6.	Duan, X., et al., *N-Doping-Induced Nonradical Reaction on Single-Walled Carbon Nanotubes for Catalytic Phenol Oxidation.* ACS Catalysis, 2015. **5**(2): p. 553-559.

7.	Wang, Y., et al., *3D-hierarchically structured MnO2 for catalytic oxidation of phenol solutions by activation of peroxymonosulfate: Structure dependence and mechanism.* Applied Catalysis B: Environmental, 2015. **164**: p. 159-167.

8.	Muhammad, S., et al., *Coal fly ash supported Co3O4 catalysts for phenol degradation using peroxymonosulfate.* RSC Advances, 2012. **2**(13): p. 5645-5650.

9.	Wei, X., et al., *Degradation of phenol with heterogeneous catalytic ozonation enhanced by high gravity technology.* Journal of Cleaner Production, 2020. **248**: p. 119179.

10.	Sarmento, A.P., et al., *Phenol degradation by Fenton-like process.* Environmental Science and Pollution Research, 2016. **23**(18): p. 18429-18438.

11.	Sun, Y., et al., *Degradation of antibiotics by modified vacuum-UV based processes: Mechanistic consequences of H2O2 and K2S2O8 in the presence of halide ions.* Science of The Total Environment, 2019. **664**: p. 312-321.

12.	Hu, L., et al., *Synthesis of FeCo nanocrystals encapsulated in nitrogen-doped graphene layers for use as highly efficient catalysts for reduction reactions.* Nanoscale, 2015. **7**(2): p. 450-454.

13.	Zhou, H., et al., *Insights into the oxidation of organic contaminants by iron nanoparticles encapsulated within boron and nitrogen co-doped carbon nanoshell: Catalyzed Fenton-like reaction at natural pH.* Environment International, 2019. **128**: p. 77-88.

14.   Wang, D., et al., *The roles of suspended solids in persulfate/Fe2+ treatment of hydraulic fracturing wastewater: Synergistic interplay of inherent wastewater components.* Chemical Engineering Journal, 2020. **388**: p. 124243.

15.   Andrew Lin, K.Y., H.A. Chang, and B.J. Chen, *Multi-functional MOF-derived magnetic carbon sponge.* Journal of Materials Chemistry A, 2016. **4**(35): p. 13611-13625.

16.   Andrew Lin, K.-Y. and Z.-Y. Zhang, *α-Sulfur as a metal-free catalyst to activate peroxymonosulfate under visible light irradiation for decolorization.* RSC Advances, 2016. **6**(18): p. 15027-15034.

17.   Lin, K.-Y.A., H.-A. Chang, and R.-C. Chen, *MOF-derived magnetic carbonaceous nanocomposite as a heterogeneous catalyst to activate oxone for decolorization of Rhodamine B in water.* Chemosphere, 2015. **130**: p. 66-72.

18.   Hu, P. and M. Long, *Cobalt-catalyzed sulfate radical-based advanced oxidation: A review on heterogeneous catalysts and applications.* Applied Catalysis B: Environmental, 2016. **181**: p. 103-117.

19.   Zhang, M.-W., et al., *Ferrocene-modified iron-based metal-organic frameworks as an enhanced catalyst for activating oxone to degrade pollutants in water.* Chemosphere, 2018. **213**: p. 295-304.

20.   Othman, I., et al., *Catalytic activation of peroxymonosulfate using CeVO4 for phenol degradation: An insight into the reaction pathway.* Applied Catalysis B: Environmental, 2020. **266**: p. 118601.

21.   Huang, Y., et al., *Enhanced peroxymonosulfate activation for phenol degradation over MnO2 at pH 3.5–9.0 via Cu(II) substitution.* Journal of Hazardous Materials, 2018. **360**: p. 303-310.

22.   Liang, H., et al., *Excellent performance of mesoporous Co3O4/MnO2 nanoparticles in heterogeneous activation of peroxymonosulfate for phenol degradation in aqueous solutions.* Applied Catalysis B: Environmental, 2012. **127**: p. 330-335.

23.   Hu, L., X. Yang, and S. Dang, *An easily recyclable Co/SBA-15 catalyst: Heterogeneous activation of peroxymonosulfate for the degradation of phenol in water.* Applied Catalysis B: Environmental, 2011. **102**(1): p. 19-26.

24.   Gao, Q., et al., *Efficient activation of peroxymonosulfate by Co-doped mesoporous CeO2 nanorods as a heterogeneous catalyst for phenol oxidation.* Environmental Science and Pollution Research, 2021.

25.   Li, L., et al., *Heterogeneous activation of peroxymonosulfate by hierarchically porous cobalt/iron bimetallic oxide nanosheets for degradation of phenol solutions.* Chemosphere, 2020. **256**: p. 127160.

26. Khan, A., et al., *Synergistic degradation of phenols using peroxymonosulfate activated by CuO-Co3O4@MnO2 nanocatalyst.* Journal of Hazardous Materials, 2017. **329**: p. 262-271.

27. Anipsitakis, G.P., E. Stathatos, and D.D. Dionysiou, *Heterogeneous Activation of Oxone Using Co3O4.* The Journal of Physical Chemistry B, 2005. **109**(27): p. 13052-13055.

28. Guo, W., et al., *Degradation of antibiotics amoxicillin by Co3O4-catalyzed peroxymonosulfate system.* Environmental Progress & Sustainable Energy, 2013. **32**(2): p. 193-197.

29. Ma, C.Y., et al., *Mesoporous Co3O4 and Au/Co3O4 Catalysts for Low-Temperature Oxidation of Trace Ethylene.* Journal of the American Chemical Society, 2010. **132**(8): p. 2608-2613.

30. Sun, Y., et al., *Exploring the Effect of Co3O4 Nanocatalysts with Different Dimensional Architectures on Methane Combustion.* 2016. **8**(3): p. 540-545.

31. Xie, X., et al., *Low-temperature oxidation of CO catalysed by Co3O4 nanorods.* Nature, 2009. **458**(7239): p. 746-749.

32. Sun, Z., T. Liao, and L. Kou, *Strategies for designing metal oxide nanostructures.* Science China Materials, 2017. **60**(1): p. 1-24.

33. Ibupoto, Z.H., et al., *Effect of Urea on the Morphology of Co3O4 Nanostructures and Their Application for Potentiometric Glucose Biosensor.* Electroanalysis, 2014. **26**(8): p. 1773-1781.

34. Cheng, G., et al., *O22-/O- functionalized oxygen-deficient Co3O4 nanorods as high performance supercapacitor electrodes and electrocatalysts towards water splitting.* Nano Energy, 2017. **38**: p. 155-166.

35. Wang, D., Q. Wang, and T. Wang, *Morphology-Controllable Synthesis of Cobalt Oxalates and Their Conversion to Mesoporous Co3O4 Nanostructures for Application in Supercapacitors.* Inorganic Chemistry, 2011. **50**(14): p. 6482-6492.

36. Zhao, S., F. Hu, and J. Li, *Hierarchical Core–Shell Al2O3@Pd-CoAlO Microspheres for Low-Temperature Toluene Combustion.* ACS Catalysis, 2016. **6**(6): p. 3433-3441.

37. Liu, Q., et al., *Dry citrate-precursor synthesized nanocrystalline cobalt oxide as highly active catalyst for total oxidation of propane.* Journal of Catalysis, 2009. **263**(1): p. 104-113.

38. Wang, X., et al., *Geometrical-Site-Dependent Catalytic Activity of Ordered Mesoporous Co-Based Spinel for Benzene Oxidation: In Situ DRIFTS Study Coupled with Raman and XAFS Spectroscopy.* ACS Catalysis, 2017. **7**(3): p. 1626-1636.

39. Hu, L., Q. Peng, and Y. Li, *Selective Synthesis of Co3O4 Nanocrystal with Different Shape and Crystal Plane Effect on Catalytic Property for Methane Combustion.* Journal of the American Chemical Society, 2008. **130**(48): p. 16136-16137.

40. Feng, L.-L., et al., *Metallic Co9S8 nanosheets grown on carbon cloth as efficient binder-free electrocatalysts for the hydrogen evolution reaction in neutral media.* Journal of Materials Chemistry A, 2016. **4**(18): p. 6860-6867.

41. Khokhra, R., et al., *Visible and UV photo-detection in ZnO nanostructured thin films via simple tuning of solution method.* Scientific Reports, 2017. **7**(1): p. 15032.

42. Shao, M., et al., *Oxygen vacancy engineering of self-doped SnO2−x nanocrystals for ultrasensitive NO2 detection.* Journal of Materials Chemistry C, 2020. **8**(2): p. 487-494.

43. Wang, Z., et al., *Surface oxygen vacancies on Co3O4 mediated catalytic formaldehyde oxidation at room temperature.* Catalysis Science & Technology, 2016. **6**(11): p. 3845-3853.

44. Dong, L., et al., *Effects of oxygen vacancies on the structural and optical properties of β-Ga2O3.* Scientific Reports, 2017. **7**(1): p. 40160.

45. de Rivas, B., et al., *Synthesis, characterisation and catalytic performance of nanocrystalline Co3O4 for gas-phase chlorinated VOC abatement.* Journal of Catalysis, 2011. **281**(1): p. 88-97.

46. Ren, Q., et al., *Controllable synthesis of 3D hierarchical Co3O4 nanocatalysts with various morphologies for the catalytic oxidation of toluene.* Journal of Materials Chemistry A, 2018. **6**(2): p. 498-509.

47. Sun, Y., et al., *Exploring the Effect of Co3O4 Nanocatalysts with Different Dimensional Architectures on Methane Combustion.* ChemCatChem, 2016. **8**(3): p. 540-545.

48. Xie, X. and W. Shen, *Morphology control of cobalt oxidenanocrystals for promoting their catalytic performance.* Nanoscale, 2009. **1**(1): p. 50-60.

49. Wachs, I.E., *Recent conceptual advances in the catalysis science of mixed metal oxide catalytic materials.* Catalysis Today, 2005. **100**(1): p. 79-94.

50. Mu, J., et al., *Intrinsic peroxidase-like activity and catalase-like activity of Co3O4 nanoparticles.* Chemical Communications, 2012. **48**(19): p. 2540-2542.

51. Trang, N.H., et al., *Cobalt ferrite nanoparticle-loaded nitrogen-doped carbon sponge as a magnetic 3D heterogeneous catalyst for monopersulfate-based oxidation of salicylic acid.* Chemosphere, 2021. **267**: p. 128906.

52. Rastogi, A., S.R. Al-Abed, and D.D. Dionysiou, *Sulfate radical-based ferrous–peroxymonosulfate oxidative system for PCBs degradation in aqueous and*

sediment systems. Applied Catalysis B: Environmental, 2009. **85**(3–4): p. 171-179.

53.   Guan, Y.-H., et al., *Influence of pH on the Formation of Sulfate and Hydroxyl Radicals in the UV/Peroxymonosulfate System.* Environmental Science & Technology, 2011. **45**(21): p. 9308-9314.

54.   Indrawirawan, S., et al., *Nanocarbons in different structural dimensions (0–3D) for phenol adsorption and metal-free catalytic oxidation.* Applied Catalysis B: Environmental, 2015. **179**: p. 352-362.